"Laser Techniques for State-Selected and State-to-State Chemistry"

Proc. SPIE - Int. Conf. Opt. Eng.
Vol. 2124 (1994).

The role of solvent and vibrations on proton tunneling in clusters

Jack A. Syage

The Aerospace Corporation
P.O. Box 92957/M5-754
Los Angeles, California 90009

ABSTRACT

In this paper we present a theoretical framework for describing the role of solvent and vibrations on proton tunneling rates. Recent experiments indicate that excited-state proton transfer in $ROH(NH_3)_n$ clusters (where ROH is 1-naphthol or phenol) occurs by a tunneling mechanism. Two previous models of proton tunneling are examined; one based on a solvent-independent bound-continuum potential and the other on a solvent-activated bound-bound potential. Here we extend the latter model to incorporate coupling of the proton to reactant and product vibrations. All three models are compared to experimental tunneling rates in clusters.

1. INTRODUCTION

Many technologies are exploiting the use of matter on smaller and smaller spatial scales (e.g., microelectronics, nanotechnology). Clusters are becoming indispensable for studying properties of the bulk on an atomic or molecular level and for understanding departures from bulk-phase behavior as the system size approaches the single-molecule gas-phase limit. Our work centers on the study of chemical reactivity in clusters using time-domain techniques. These discussions will focus on excited-state proton transfer reactions (ESPT) of the form

$$ROH^* \cdots B_n \underset{k}{\longrightarrow} [RO^{*-} \cdots H^+B_n]_{ur} \underset{k_s}{\longrightarrow} [RO^{*-} \cdots H^+B_n]_r$$

where ROH is an aromatic acid (e.g., 1- and 2-naphthol, and phenol), B is a base-type solvent molecule, and n is the number of solvent molecules in the cluster. We assume a two-step process involving initial proton transfer followed by solvent reorganization from an unrelaxed ur to a relaxed r configuration. Due to the growing number of studies, ESPT in clusters is developing into a prototype for evaluating the role of individual solvent molecules on chemical reactivity. Leutwyler and coworkers (e.g., Cheshnovsky and Knochenmuss) initiated the study of ESPT in clusters in a series of experiments on 1- and 2-naphthol (henceforth NpOH) that revealed distinct threshold size dependences that varied with solvent proton affinity.[1,2] Tramer *et al.* reported threshold behavior for phenol (henceforth PhOH) by measuring changes in ionization potentials with n.[3] These studies provided valuable spectroscopic data and details regarding the thermochemistry of ESPT. Picosecond time-resolved measurements were conducted by Zewail and coworkers for 1-NpOH,[4] by Bernstein, Kelley, and coworkers for protio and deutero 1-NpOH,[5] and by Steadman and Syage for protio and deutero PhOH.[6–10] In these experiments, rates of proton transfer were measured by resonance ionization mass spectrometry for various solvents and cluster size. Knochenmuss *et al.*[11] measured ESPT in 1-$NpOH(H_2O)_n$ by picosecond fluorescence spectroscopy for medium to large cluster sizes and Hineman, Kelley, and Bernstein[12] reported on fragmentation in $PhOH(NH_3)_n$ using picosecond multiphoton ionization. ESPT involving aromatic acids have been studied extensively in the condensed phase including several time-resolved experiments,[13–15] which gives a valuable base of

information for comparing to cluster results.

In the following we present a discussion on the dynamics of tunneling. An attempt is made to frame the subject in the context of condensed-phase tunneling theory. We will discover, though, that small solvent clusters do not behave as bulk solvent, but neither do they follow gas-phase behavior. To bridge this gap we propose a model for incorporating solvent and vibrational interactions.[16–18] The intent of this work is to open discussion on how to model reactivity and solvation in small clusters.

Details of the measurements are described in the section called Experimental Methods. This is followed by a Background section that summarizes experimental results from our laboratory and related work by others. We then describe in a section called Barrier Models how the potential energy diagram for ESPT in clusters is derived and examine the barrier properties along the O–H, the O···N, and the solvent coordinates. Under Tunneling Models, we present details of two different pictures of tunneling and propose an approach that consolidates the different viewpoints. In Comparison to Experiment, we compare the various models to each other and to available data for ESPT in clusters.

2. EXPERIMENTAL METHODS

In a typical experiment, a molecular beam of clusters is photoexcited to a reactive state by a pump pulse and the evolution of some property (e.g., relaxation, spectral shifts, or reactant decay and product formation) is monitored by a variably-delayed probe pulse using multiphoton ionization. Most of our experiments use a time-of-flight mass spectrometer in order to measure dynamics as a function of cluster size.[6–10,19,20] More recently, we have applied time-resolved photoelectron spectroscopy (TR/PES) to the measure of dynamical properties in clusters.[10,21] Details of the experiments can be found in the source papers and review articles. Time-resolved techniques used by other groups to study chemistry in clusters include laser-induced fluorescence and cluster ion photodissociation.[22–25]

A qualitative picture of the cluster potential energy curves for ground, excited, and ionic states is given in Fig. 1 along with the picosecond pump-probe excitation/detection scheme used to measure the chemical rates. Figure 1 also shows representative ion energy distributions, measurable by photoelectron spectroscopy. Reactant and product are distinguishable in our experiments by mass spectrometry because they fragment differently upon ionization. Ionization of reactant clusters $PhOH^* \cdots B_n$ produces cluster ions $PhOH^+ \cdots B_n$ on the inner potential well where the O–H coordinate is strongly bound. Conversely, ionization of the product ion-pairs $PhO^{*-} \cdots H^+B_n$ produces cluster ions $PhO \cdots H^+B_n$ on the outer well where facile dissociation occurs to give H^+B_n. The observed reactant and product signals show matching kinetics, which is important for establishing that the observed response is a proton transfer reaction.

3. BACKGROUND

The driving force behind ESPT is the proton affinity of the solvent cluster. The simplest view is that RO^{*-} and B_n compete for the proton and that the reaction free energy $\Delta G_{0,n}$ depends on the proton affinity of these two moieties. Thermochemical cycles, based on this principal, have proved useful for describing the qualitative dependence of reactivity on properties of the solvent B_n. Some attempts have been made to include other interactions (e.g., Coulombic interactions)[6] and to model the potential energy surface along a few relevant coordinates (e.g., O–H and solvent coordinate),[9] but rigorous theoretical calculations of the reaction energetics are lacking. Nonetheless, experimental results have clarified many properties of ESPT in clusters. Some important conclusions are as follows:

(1) The solvent proton affinity increases in fairly large discrete steps for the addition of the first few solvent molecules (and $\Delta G_{0,n}$ decreases in a similar stepwise manner). As the cluster grows in size, the

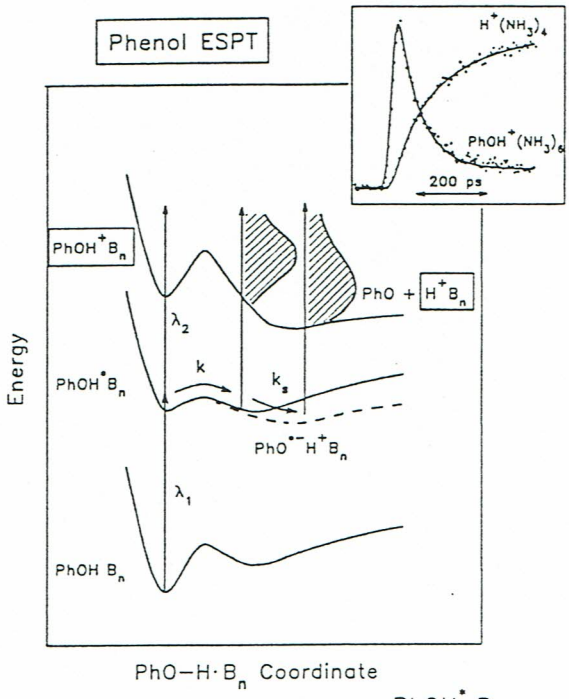

Figure 1. Energy diagram for $PhOH(NH_3)_n$ consistent with a cluster size of $n \sim 5$. The pump and probe pulses are denoted as λ_1 and λ_2, and the ESPT and solvent reorganization rate constants are given by k and k_s, respectively. The expected photoelectron band shapes resulting from these processes is also shown. The ion signals for reactant and product are given in the insert and show matching kinetics. A lower n value for the product is plotted to reflect the loss of two NH_3 that evaporate on average in the dissociative ionization step (Refs. 6 and 19b).

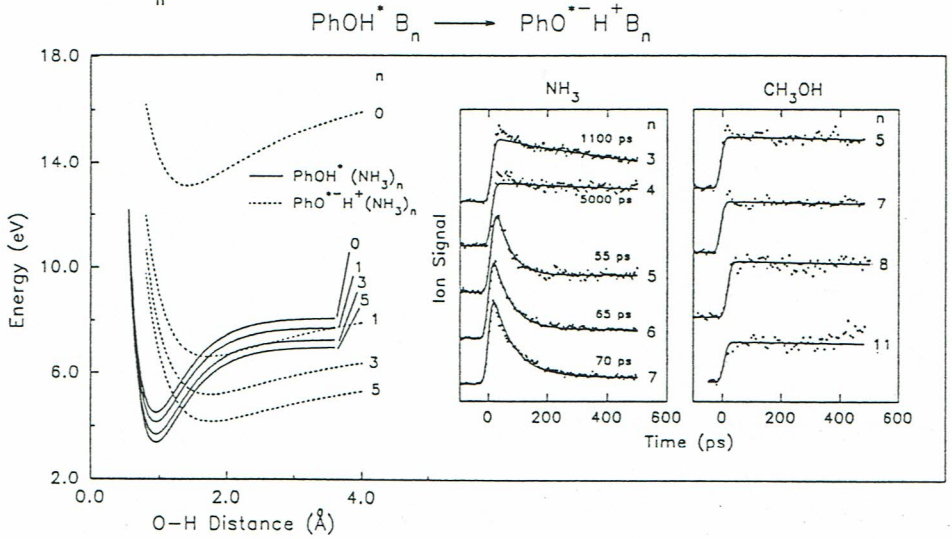

Figure 2. Approximate $PhOH(NH_3)_n$ cluster potential energy curves for the reactive PhO–H coordinate. These curves assume an equilibrium O···N bond distance (approximately 1.8 Å and 1.0 Å for the neutral and ion-pair states, respectively). Insert shows observed lifetime of the reactant $PhOH^*B_n$ (as measured by $PhOH^+B_n$ detection) in solvent clusters $(NH_3)_n$ and $(CH_3OH)_n$ at 2500 cm^{-1} internal energy. The calculated curves are described in Refs. 6 and 20. Calculated curves for the $(CH_3OH)_n$ data assume a 10 ns lifetime.

steps become smaller and proton affinity converges to the bulk-phase limit (basicity). For strong base molecules where reaction occurs for small n (e.g., NH_3) a change from positive to negative free energy can occur by addition of a single solvent molecule. This explains the sharp size thresholds for ESPT observed for many systems.[1–8] An example of this effect is given in Fig. 2, which shows in the time-domain that photoexcitation of $PhOH(NH_3)_n$ leads to a distinct onset to reaction at $n = 5$.[6,20] Similar measurements on 1-$NpOH(NH_3)_n$ show an onset at $n = 3$ reflecting the greater acidity of 1-NpOH relative to PhOH.[4,5]

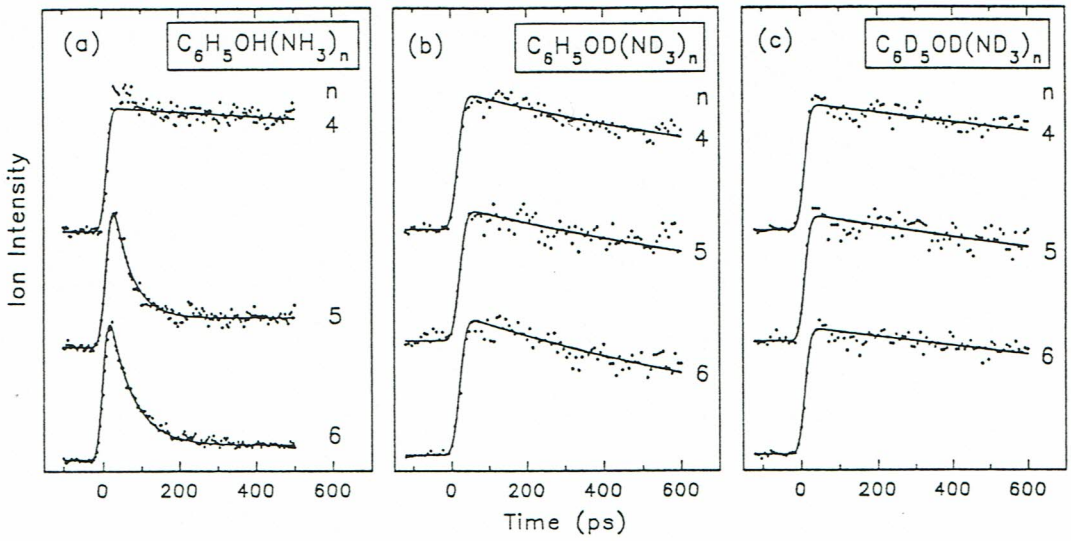

Figure 3. The effect of deuteration on the excited-state lifetime of phenol$(NH_3)_n$ $n = 4 - 6$. The data were fitted to single-exponential functions with the following lifetimes: (a) 5.0 ns ($n = 4$), 55 ps ($n = 5$), 65 ps ($n = 6$); (b) 1.5 ns ($n = 4$), 1.5 ns ($n = 5$), 1.1 ns ($n = 6$); (c) 2.4 ns ($n = 4$), 2.0 ns ($n = 5$), 2.4 ns ($n = 6$).

(2) ESPT rates increase gradually with excess energy in 1-NpOH$(NH_3)_n$ indicating a barrier process.[5] A rate constant of about $(60\ \text{ps})^{-1}$ for PhOH$(NH_3)_n$ at 2500 cm^{-1} of excess energy also suggests a barrier impedence to reaction.[6] A model of the potential energies indicates that the proton transfer state derives from a high-lying charge-transfer state of phenol. The stabilization of this state by successive addition of solvent molecules is diagrammed in Fig. 2.

(3) A strong proton/deuteron isotope effect on rates for 1-NpOH[5] and PhOH[9] in $(NH_3)_n$ solvent clusters indicates that proton transfer occurs by tunneling. For example ESPT lifetimes for $C_6H_5OD(ND_3)_n$ and $C_6D_5OD(ND_3)_n$ range from 1–2.5 ns for $n = 5$ and 6 versus about 60 ps for $C_6H_5OH(NH_3)_n$ as shown in Fig. 3.[9] The observation of ESPT from the vibrationless levels of 1-NpOH$(NH_3)_n$ also supports a tunneling mechanism.[4,5]

(4) The proton is strongly coupled to the product and solvent modes as evidenced by a large solvent structural change that occurs after proton transfer. In separate time-resolved experiments using mass spectrometry[6] and photoelectron spectroscopy,[10] we measured a solvent reorganizational time constant of about 300 ps for initially formed $PhO^{*-}H^{+}(NH_3)_n$. The photoelectron spectrum, shown in Fig. 4, evolved in time due to the geometry change. The magnitude of the shift is significant indicating a solvent reorganization energy of about 0.5 eV.

The experimental results have contributed to a better understanding of the barrier properties of ESPT, however, important questions still remain regarding the dynamics of proton tunneling, such as

(1) Is the energy dependence of k attributable solely to the O–H tunneling barrier and the probability of populating the important O$\cdots$N mode as assumed by the Hineman *et al.* (HBKB) model, or are solvent and vibrational dynamics also important? The energy dependence is well described by the HBKB bound-continuum model, however, is this a unique description?

(2) Why is k relatively invariant to n (cf. Fig. 2)? This insensitivity has now been observed by three groups for 1-NpOH[4,5] and PhOH[6,9] in $(NH_3)_n$. Neither tunneling model thus far used to describe ESPT predicts this effect.

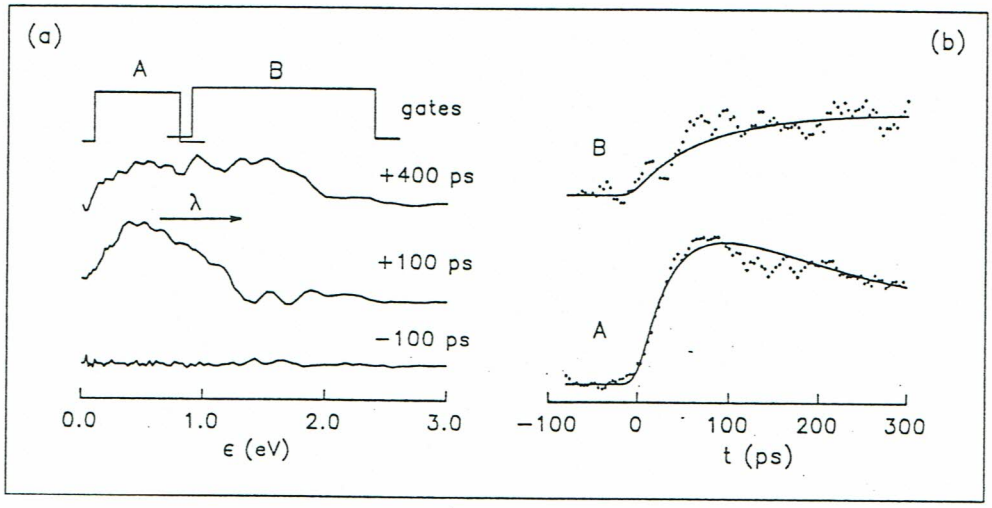

Figure 4. Time-resolved photoelectron spectra as a function of pump-probe delay time t. (a) Difference spectra corresponding to (pump + probe) − (pump). Gate widths are constant in time. (b) Observed time-dependences of the low-energy (gate A) and high-energy (gate B) photoelectron bands are plotted. Fitted curves were calculated for rate constants $k = (50\ \text{ps})^{-1}$ and $k_s = (300\ \text{ps})^{-1}$ and spectral parameters discussed in Ref. 10.

4. BARRIER MODELS

The ion-pair product potential derives from a charge-transfer or ion-pair state of isolated phenol that corresponds to the dissociative limit $PhO^{*-} + H^+$.[6,20] This state is stabilized significantly by molecules with high proton affinity as shown by the energy diagram in Fig. 2. This simple picture predicts a surface crossing along the O–H coordinate with the initially excited S_1 Coulombic state of phenol. It also predicts that ESPT becomes exoergic for some minimum, but small, number of NH_3 molecules. The simple model is intuitive, but neglects other stabilizing interactions, which explains why the predicted and observed onset values of n differ.

Proton tunneling in clusters has recently been described by two conceptually different models; the first developed by Hineman *et al.* (HBKB)[5] is based on a bound-to-continuum proton transition (Fig. 5a) and the second proposed by us is based on a bound-to-bound proton transition (Fig. 5b) mediated by solvent motion (condensed-phase picture).[9] Both models use Bell theory for the tunneling interaction[26] and obtain good predictions of the proton/deuteron isotope effect. The bound-continuum model obtains good agreement with the dependence of k on internal energy E, but fails to describe the dependence of k on cluster size (i.e., reaction free energy ΔG_0). The solvent-activated bound-bound model obtains only fair agreement on E and ΔG_0. The difference between the two models is in how they treat the density of product states coupled to the reactive O–H coordinate. The former model is simplistic in assuming a continuum of product states (Fig. 5a) and therefore suffers from too broad a density of states. The latter model (Fig. 5b), though fundamentally more realistic, suffers from too narrow a density of states by assuming coupling to only the vibrationless N–H stretch mode of the product. In real systems one expects many vibrations in the product to couple to the proton, the effect of which is to broaden the density of accepting states to an extent determined by Franck-Condon relations. This possibility is illustrated by the barrier picture in Fig. 5c.

A minimum of four nuclear coordinates are needed to properly discuss proton tunneling: (1) the O–H coordinate q_H, which is the reaction coordinate, (2) the O···N coordinate Q_N, in which the O···N symmetric stretch modulates the internuclear distance between potential minima, which in turn modulates

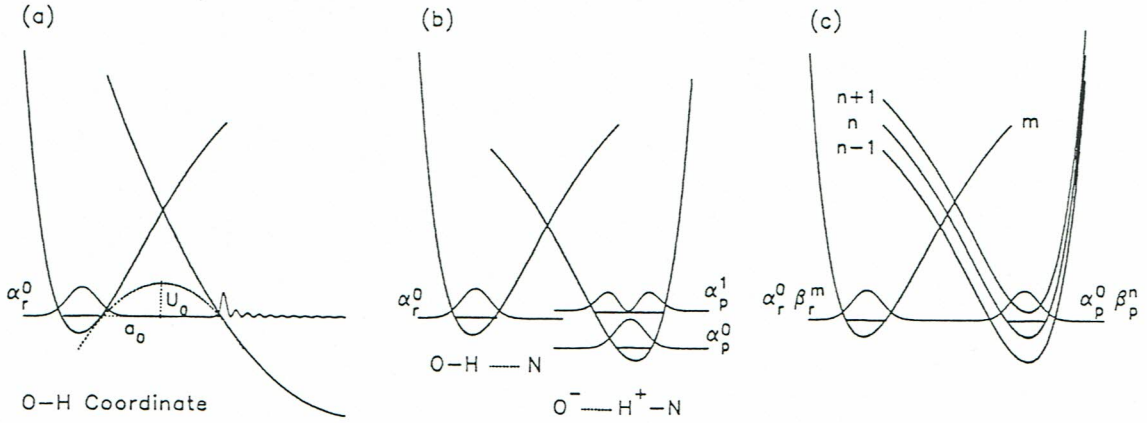

Figure 5. (a) Bound-continnum potential, (b) bound-bound potential, and (c) bound-bound potential with vibrational energy shifts plotted along the O–H coordinate. Vibrational wavefunctions for the O–H oscillator are denoted by α where the subscripts r and p refer to reactant and product, and the superscript denotes number of quanta. β_r^m and β_p^n refer to a reactant (m quanta) and product (n quanta) vibration that couples to proton translocation. Diabatic curves are shown. An inverted paraboloic barrier (avoided crossing) of height U_0 and half width a_0 is used for calculations.

the barrier height and width, (3) the solvent coordinate S, in which solvent modes cause fluctuations in the relative energies of reactant and product, and (4) coordinates corresponding to product accepting modes that reduce the electronic energy gap between reactant and product.[9] All coordinates, except for S, are treated quantally. We begin in Fig. 5b with a schematic representation of the bound Coulombic and ion-pair potentials along the O–H coordinate for a fixed O$\cdots$N and solvent coordinate. The example given in Fig. 5b is for an asymmetric double well (e.g., different minima energy). Vibrational probability functions are drawn for the O–H and N–H vibrationless levels of the reactant and product, α_r^0 and α_p^0, respectively, and for the $v = 1$ level of the product α_p^1. For the asymmetric potential the vibrational wavefunctions are localized in either well with miniscule probability *leaking* into the other well. In this case the tunneling probability is insignificant.

Condensed-phase theories of proton tunneling, such as those of Borgis and Hynes,[16] and Cukier and Morillo,[17] assume that tunneling occurs when the solvent through thermal fluctations achieves critical but momentary configurations for which the potential wells become symmetric. Under these conditions where the zeroth-order vibrational energies are degenerate, the tunneling interaction is strongest (i.e. tunneling splitting) and the vibrational probabilities become delocalized over both potentials. In other words, the tunneling probability is maximized. A similar tunneling enhancement would occur if the α_r^0 and α_p^1 zeroth order states became degenerate. The concept of solvent fluctuations creating momentary symmetric potentials is based on Marcus theory of electron transfer.[27,28]

The critical solvent configurations $S^\ddagger$ for achieving the symmetric potential for tunneling will most likely be different from the equilibrium solvent geometries of the reactant and product states, S_r and S_p, respectively. Schematic representations of the The O–H potential for S_r and S_p are given in Fig. 6a. This picture is important because it implies that an exoergic reaction occurs only if there is solvent motion to reduce the energy of the product state. A convenient way to represent the solvent activation energy is to plot the minimum energies of the reactant and product potentials as a function of solvent coordinate S as shown in Fig. 6b. This view indicates that there is an activated solvent configuration $S^\ddagger$ at energy $\Delta G^\ddagger$ for bringing the reactant and product minimum energies (or vibrationless levels) into resonance. The difference in the energy of the product for the solvent geometries S_r and S_p is sometimes referred to as the solvent reorganization energy λ_S, and is a quantity we measure by time-resolved photoelectron

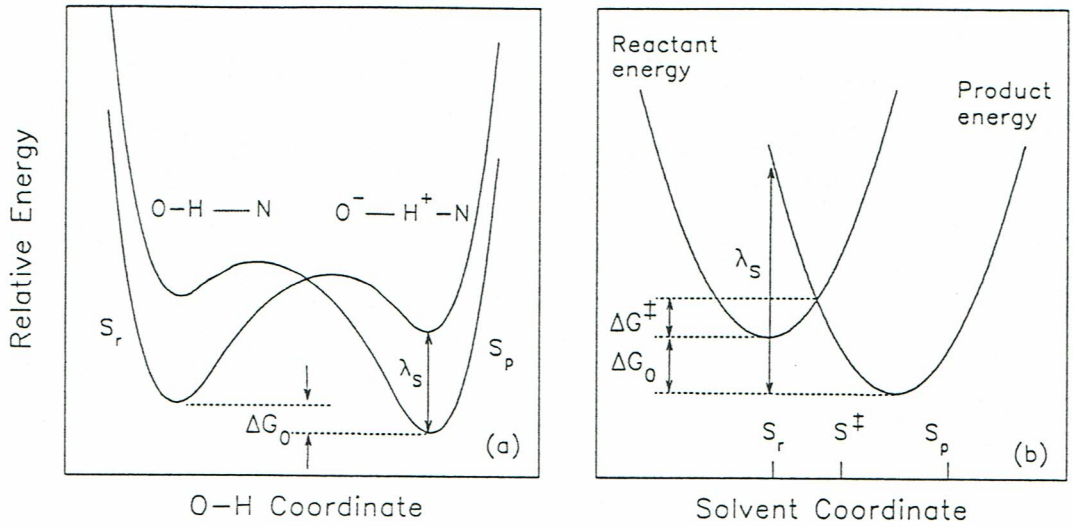

Figure 6. (a) Schematic representation of the potential energy along the O–H coordinate for fixed solvent configurations S_r and S_p. (b) Reactant and product minimum energy as a function of solvent coordinate S. $\Delta G^{\ddagger}$ is the free energy of activation for achieving resonance between the reactant and product minimum (vibrationless) energy. ΔG_0 is the free energy of reaction for an equilibrating solvent. λ_S is the solvent reorganization energy.

spectroscopy.[6]

It is apparent from Fig. 5b that large solvent fluctuations are necessary to achieve tunneling resonances because of the large energy gap between reactant and product. This leads to predicted temperature dependences that are much steeper than observed in bulk and in clusters and to a predicted slowing of tunneling rates for large exoergicities (i.e., Marcus inverted region) that are rarely observed. This problem is circumvented by considering other vibrations β that couple to the O–H coordinate (e.g., O$\cdots$N stretch and solvent-solvent bending modes) to reduce energy gaps between reactant and product as depicted in Fig 5c by the combination states $\alpha_r^0\beta_r^m$ and $\alpha_p^0\beta_p^n$. A similar series of product curves should be envisioned for Figs. 6a and 6b. In reality a quasicontinuum of states may exist to provide additional bridging of energy gaps between reactant and product. Modeling the vibrational manifold is important because the smaller the reaction energy gap, the less important is solvent motions for bring reactant and product into resonance.

5. TUNNELING MODELS

We reported in a previous study a detailed comparison of the bound-continuum and solvent-activated bound-bound proton tunneling.[9] We reiterate essential features and then show how vibrations are incorporated into the latter model. The two models of tunneling can be compared by the following rate equations

$$W_{r\to p} = \nu_H \exp[-2\Omega] \qquad \text{(bound-continuum transition)} \tag{1}$$

$$W_{r\to p} = \frac{h\nu_H^2}{2}\exp[-2\Omega]\left(\frac{\beta}{\pi\lambda_S}\right)^{1/2}\exp[-\beta\Delta G^{\ddagger}]$$

$$\text{(solvent-activated bound-bound transition)} \tag{2}$$

where ν_H is the O–H vibrational frequency and

$$\Omega = \frac{\pi^2 a}{h}(2mU)^{1/2} \tag{3a}$$

$$\Delta G^{\ddagger} = (\Delta G_0 + \lambda_S)^2/4\lambda_S \tag{3b}$$

$$\beta^{-1} = (k_b T + E_{vib}/s) \tag{3c}$$

The terms in Ω and $\Delta G^{\ddagger}$ are defined in Figs. 3 and 4. T is the initial cluster temperature (k_b is the Boltzmann constant), E_{vib} is the vibrational excitation energy in S_1, and s is the number of effective degrees of freedom in the cluster that contribute to the heat capacity. β^{-1} is loosely defined as an energy per effective degree of freedom. (We use linear not angular frequency units throughout, i.e., s^{-1}.)

It is useful to cast the above equations as Golden Rule type equations of the form

$$W_{r\to p} = \frac{4\pi^2}{h} C^2 \rho \tag{4}$$

in order to separate the terms associated with the coupling C and the effective density of states ρ. The tunneling splitting for an O–H symmetric double-well potential with an inverted parabolic barrier is given by[22]

$$2C = \frac{h\nu_H}{\pi} \exp[-\Omega] \tag{5}$$

Using Eqs. (4) and (5) it is possible to sort out the terms in Eqs. (1) and (2) that correspond to an effective density of states as follows:

$$\rho = \frac{1}{h\nu_H} \qquad \text{(bound-continuum transition)} \tag{6}$$

$$\rho = \frac{1}{2}\left(\frac{\beta}{\pi\lambda_S}\right)^{1/2} \exp[-\beta\Delta G^{\ddagger}] \qquad \text{(bound-bound transition)} \tag{7}$$

The reaction free energy ΔG_0 is the driving force for proton transfer. Eq. (7) is identical to that obtained from the classical Marcus theory of electron transfer.[27] The dependence of ρ on ΔG_0 is vastly different by the two models; it is a constant value for the bound-continuum case and a strongly peaked function about the value λ_S for the bound-bound case. The latter case is plotted in Fig. 7a for different internal energies β^{-1}. Since W is directly proportional to ρ, Figure 7a predicts a rate that peaks at $\Delta G_0 = -\lambda_S$ and then decreases with increasing exoergicity. This behavior is the so called Marcus inverted region. A second outcome of the peaked density function is a potentially large temperature dependence. Oddly, the temperature dependence becomes negative as $-\Delta G_0/\lambda_S$ approaches unity. For comparison, the value of ρ by Eq. (6) is indicated in Fig. 7 by the arrow.

The peculiar behavior predicted by Eq. (7) (and classical Marcus theory of electron transfer) is generally moderated in real systems by the coupling of the proton to vibrational modes other than O–H and N–H as depicted by the coupling of the reactant potential to a manifold of product potentials in Fig. 5c. Coupling refers to vibrations that undergo changes in quantum number due to proton transfer (e.g., mode β in Fig. 5c).[27–29] Eq. (7) is then modified to include a sum over a Franck-Condon probability distribution for change in quantum number, i.e.,

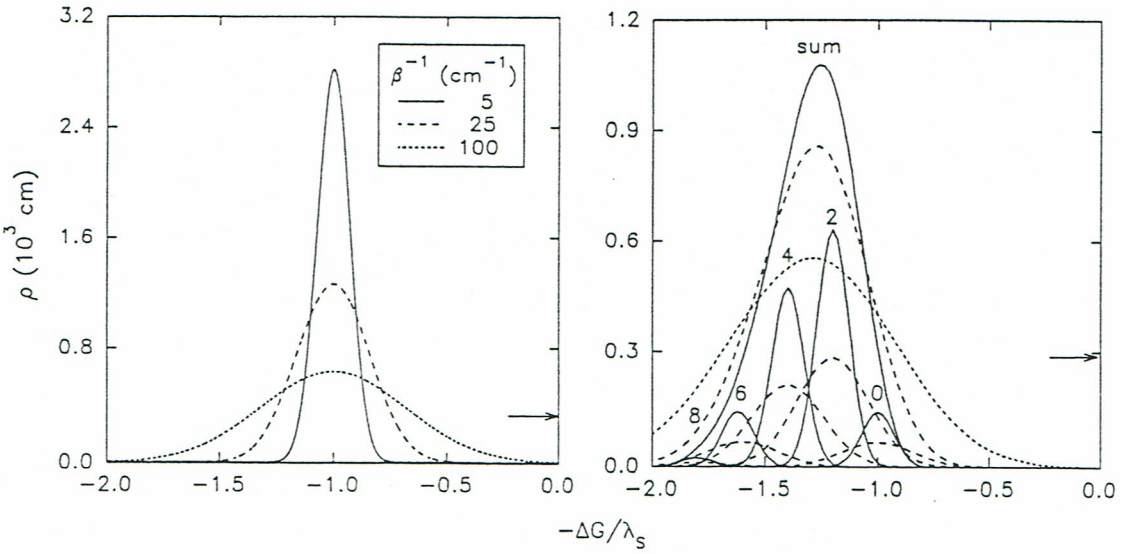

Figure 7. Calculated density of states as a function of driving force ΔG_0. (a) coupling of O–H and N–H vibrationless levels only. (b) coupling of O–H to a Franck-Condon distribution of an accepting mode ν originating from $m = 0$. Individual n components are shown along with the sum according to Eq. (8). Different values of internal energy are represented by β^{-1}. Other parameters are $\lambda_S = 2000\ \text{cm}^{-1}$, $\lambda_\nu = 600\ \text{cm}^{-1}$, and $h\nu = 200\ \text{cm}^{-1}$. The arrow at a value of 0.00029 represents ρ for the bound-continuum model.

$$\rho_{\{m\}} = \frac{1}{2}\left(\frac{\beta}{\pi\lambda_S}\right)^{1/2} \sum_{n_1=0}^{\infty} \cdots \sum_{n_M=0}^{\infty} \prod_{i}^{M} |\langle m_i|n_i\rangle|^2 \exp[-\beta\Delta G^{\ddagger}_{m_i,n_i}] \qquad (8)$$

(vibrational and solvent-activated tunneling)

where M is the number of coupled modes and

$$\Delta G^{\ddagger}_{m_i,n_i} = \frac{1}{4\lambda_S}\left[\Delta G_0 + \lambda_S + \sum_i (n_i - m_i)h\nu_i\right]^2 \qquad (9a)$$

$$|\langle m|n\rangle|^2 = m!n!\exp(-Z)\left|\sum_{q=0}^{\min(m,n)} (-1)^{n-q}\frac{Z^{(m+n-2q)/2}}{q!(m-q)!(n-q)!}\right|^2 \qquad (9b)$$

$$Z_i = \lambda_i/h\nu_i \qquad (9c)$$

(we have dropped the subscript i in Eq. (9b) for clarity). The function $\rho_{\{m\}}$ is defined as the effective density of product states coupled to reactant state $\prod_i |m_i>$. Eq. (9b) are Franck-Condon factors for displaced harmonic oscillators. A more rigorous treatment that includes mode distortions and anharmonicities is deemed unwarranted at this time. It is worth noting that Eq. (9b) simplifies considerably for $m = 0$ to give $|\langle 0|n\rangle|^2 = e^{-Z}Z^n/n!$. Our use of multidimensional Franck-Condon factors for modeling the density of vibrational accepting states follows from radiationless decay theory.[29] The terms λ_i are the quantum vibrational reorganization energies and are analogous to the classical parameter λ_S for solvent, except that former values are expressed per mode whereas the latter value is a sum over the classical intermolecular solvent modes. More formally,

$$\lambda_i = 2\pi\mu_i\nu_i^2\Delta q_i^{o}/h \tag{10}$$

where Δq_i^o is the change in equilibrium distance for mode i in going from reactant to product. An accepting mode that is strongly coupled to the reaction coordinate will have a large Δq_i^o, hence, λ_i is a parameter that represents the strength of coupling to the reactive proton.

To visualize how the effective density of states is broadened by vibrational coupling, we plot Eq. (8) as a function of driving force ΔG_0 in Fig 7b for the case of a single accepting mode originating from $m = 0$. Individual n terms in the summation are also shown. An inspection of Figs. 7a and 7b lead to the following conclusions concerning vibrational coupling: [1] the dependence of W with ΔG_0 is less sensitive particularly in the inverted region, and [2] the dependence of W with β^{-1} (temperature effect) is also less sensitive. Inclusion of other modes would lessen these dependencies even further. Finally, we note that summing W over a distribution of initial states $\prod_i |m_i\rangle$ would shift density of product accepting states to the region $-\Delta G_0/\lambda_S < 1$, thereby reducing the strong temperature dependence at these energies.

We simplify Eq. (8) for the purpose of comparing to experiment by considering just two dominant accepting modes and grouping the remaining modes as a weakly coupled quasicontinuum. For a linear O$\cdots$H$\cdots$N hydrogen bond we expect the N–H (ν_H = 3000–3500 cm^{-1}) and O$\cdots$N (ν_N = 100–300 cm^{-1}) stretch vibrations to be strongly coupled to the reaction coordinate. Within the quasicontinuum, only the lowest frequency modes ($\nu < \nu_N$) are effective at reducing the energy gaps further. We assign a collective frequency ν_L to s' number of oscillators where Eq. (9c) now becomes $Z_L = s'\lambda_L/h\nu_L$. Alternative methods for treating the quasicontinuum of low frequency oscillators would be worth exploring such as the use of a classical expression or some form of an energy gap law.

Figure 8 serves as a final illustration of the role of vibrational coupling on the probability of tunneling. Here we show the individual Franck-Condon and Boltzmann terms that comprise $\rho_{\{m\}}$ in Eq. (8) and Fig. 7. We consider only the ν_N and ν_H modes for clarity. Franck-Condon distributions are presented in Fig. 8 for different values of the coupling strength λ_N and the number of quanta in the reactant m_n. The distribution of accepting states becomes more continuous as λ_N and m_N increase. A more continuous distribution would also arise if other modes, such as ν_L, were included. The distribution in the absence of vibrational coupling (solvent-only model) corresponds to a single spike at zero energy. The probability of the reactant state being resonant with a product accepting state (i.e., tunneling resonance) is given by the Boltzmann term in Eq. (8). This function is plotted in Fig. 8 for two different values of the driving force ΔG_0 and the cluster energy content β^{-1}. As explained earlier, the probability of a tunneling resonance diminishes rapidly as $\Delta G_0 + \lambda_S$ deviates from zero in the absence of vibrational coupling. However, as the distribution of accepting modes in the product broadens, the probability of the Boltzmann function overlapping with a product state becomes less dependent on ΔG_0, λ_S, and β^{-1}. The HBKB bound-continuum model, which has no dependence on these parameters, would correspond to the limit where the distribution of states is continuous and uniform.

The promoting mode (averaging over Q_N): The tunneling splitting or probability is enhanced considerably by vibrations that compress the O$\cdots$N distance, thereby reducing the barrier height and width. Most effective is the intermolecular O$\cdots$N symmetric stretch mode. The details of this treatment have been reported by HBKB and later by us.[5,9] We evaluate the tunneling rate constant k as a function of O$\cdots$N distance and integrate over the wavefunction for m quanta of O$\cdots$N stretch, i.e.,

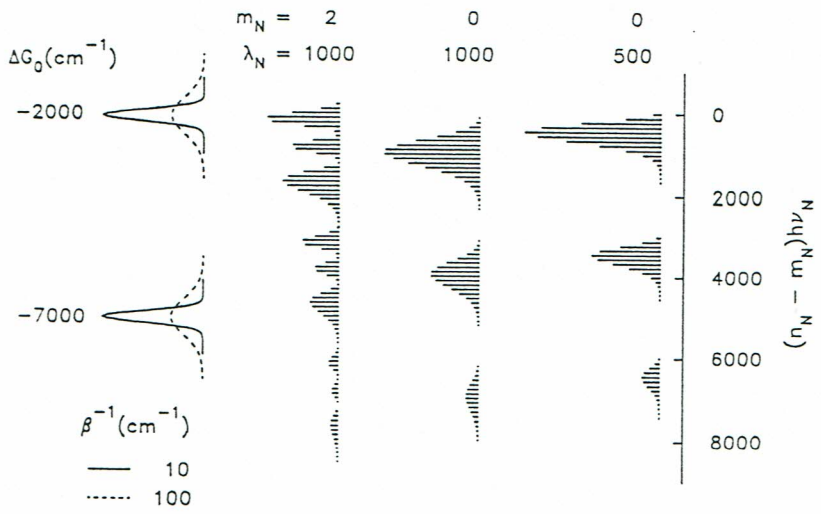

Figure 8. A representation of how the Franck-Condon distribution of product accepting states depends on λ_N and m_N. The Boltzmann term in Eq. (8) is given for different values of ΔG_0 and β^{-1}. Other parameters used in calculation are: $\nu_N = 110$ cm^{-1}, $\nu_H = 3000$ cm^{-1}, and $\lambda_H = 1500$ cm^{-1}, and $\lambda_S = 2000$ cm^{-1}

$$\begin{aligned} k_m &= \langle\psi_m|W(x)|\psi_m\rangle \\ &= \frac{4\pi^2}{h}\langle\psi_m|C(x)^2|\psi_m\rangle\rho_m \\ &= \frac{4\pi^2}{h}\rho_m\int_{-\infty}^{\infty} C(x)^2 f_m(x)dx \end{aligned} \tag{11}$$

where x is the deviation of the O$\cdots$N distance from the equilibrium position. The $C(x)^2$ dependence derives from the $a(x)$ and $U(x)$ dependences, which are easily evaluated for a parabolic barrier.[30] The O$\cdots$N vibrational amplitude probability $f_m(x)$ is given by

$$f_v(x) = |\psi_v|^2 = \left|N_v H_v(\alpha^{1/2}x)\exp(-\alpha x^2/2)\right|^2 \tag{12}$$

where

$$N_v = \left[\frac{1}{2^v v!}\left(\frac{\alpha}{\pi}\right)^{1/2}\right]^{1/2} \tag{13a}$$

$$\alpha = \frac{4\pi^2\mu\nu_2}{h} \tag{13b}$$

and ν_2 is the O$\cdots$N oscillator frequency and $H_v(\alpha^{1/2}x)$ are the Hermite polynomials. Substituting Eqs. (12) and (13) into Eq. (11) gives the expression

$$k_m = \gamma N_v^2\frac{h\nu_N}{2}\rho_m\int_{-\infty}^{\infty} H_v(\alpha^{1/2}x)^2\exp(-px^2+2qx)dx \tag{14}$$

where

$$\gamma = \exp(2qa_o) \tag{15a}$$

$$q = -\frac{\pi^2}{h}(2mU_o)^{1/2} \tag{15b}$$

$$p = \alpha - q/2a_o \tag{15c}$$

Eq. (14) can be integrated analytically; however, the computation becomes extremely tedious for increasing v because of the squared Hermite polynomial term. We used a symbolic algebra routine to evaluate Eq. (14) up to $v = 5$.[31] The resulting expressions are used for all three tunneling models above.

The density of state functions given by Eqs. (6) and (7) are independent of the integration over the O···N vibrational Q_N coordinate (i.e., $\rho_m = \rho$). For the case of vibrational-coupling [Eq. (8)], we include the O···N promoting mode as a dominant product accepting mode of frequency ν_N. This approach was used by Borgis and Hynes in a semiclassical treatment of vibrational coupling.[16]

The rate constant as a function of internal energy ($E = s\beta^{-1}$) is obtained by the expression

$$k(E) = \sum_m P_m(E)k_m \tag{16}$$

where $P_m(E)$ is the population probability of m quanta of O···N stretch at energy E. $P_m(E)$ is evaluated using a classical expression for calculating $P_m(E)$ based on the Marcus-Rice approximation[32]

$$P_m(E) = \frac{[(E - E_m)/E]^{s-2}}{\sum_m [(E - E_m)/E]^{s-2}} \tag{17}$$

where E_m is the energy of the specific vdW mode (i.e., the O···N stretch fundamental frequency) and s as defined earlier is the number of effective degrees of freedom. We assume that only intermolecular vibrational and rotational (or reorientational) modes are of sufficiently low frequency to be effective oscillators in low temperature clusters[33] and, therefore, define $s = 6(n+1) - 6$ where $n+1$ is the number of molecules in the clusters $ROH(NH_3)_n$. All other modes (i.e., intramolecular modes) are assumed to be of significantly higher frequency to be significantly less important to the effective density of states.

6. COMPARISON WITH EXPERIMENTS

Comparison of the models to experiment is hampered because many of the parameters in the above expressions are not experimentally well-defined. In the following we wish to simply compare the different tunneling models to better understand their strengths and weaknesses. The comparison to experimental data is presented to test the response of each model to different experimental variables such as internal energy and reaction driving force. It is premature to attach quantitative significance to the calculations, however, we expect to achieve some reasonable predictions of qualitative trends.

Calculated results for the three tunneling models outlined here are compared to experiment in Figs. 9 and 10. HBKB measured tunneling rates as a function of vibrational energy for 1-$NpOH(NH_3)_n$ and 1-$NpOD(ND_3)_n$, $n = 3$ and $n = 4$.[5] They reported good agreement between experiment and the bound-continuum tunneling model for $n = 3$. We have duplicated their calculations in Fig. 9. (After correcting their equations for minor errors, a value of $a_0 = 0.214$ Å was required to reproduce their results for $a_0 = 0.20$ Å. The correction has led to an increase in the k_H/k_D isotope effect, but the agreement with

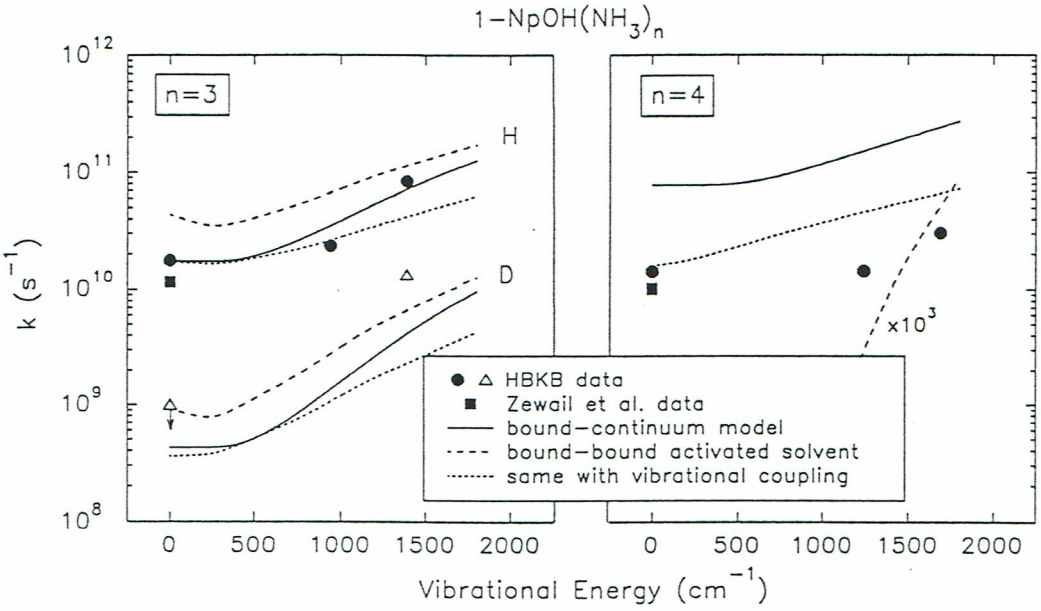

Figure 9. Calculated energy dependence of k by the three models of tunneling and comparison to measurements for 1-NpOH$(NH_3)_n$ and 1-NpOD$(ND_3)_n$. Parameters for calculations (n= 3 and 4, respectively) are: $\nu_H = 3000$ cm^{-1} (O–H), 2122 cm^{-1} (O–D); $\nu_N = 110$, 99 cm^{-1}; $\mu_N = 38, 46$ amu; $U_0 = 0.81$, 0.66 eV; $a_0 = 0.214$, 0.193 Å; $s = 18, 24$; $k_bT = 13$ cm^{-1}, $\lambda_H = 1500$ cm^{-1}, $\lambda_N = 1000$ cm^{-1}, $\lambda_L/s' = \lambda_S/s = 50$ (n=3) and 40 cm^{-1} (n=4) where $s' = s/4$ is chosen arbitrarily. $\Delta G_0 =$ –2200, –4700 cm^{-1}. The values of a_0 and U_0 are different for the O–H and O–D oscillators because the vibrationless levels lie at different energies. For the solvent-only model λ_S is interpreted as a collective solvent reorganization energy and has a value augmented by the low frequency contribution $\lambda_N + s'\lambda_L$.

experiment is still acceptable.) To calculate $k(E)$ for $n = 4$ we assume that the barrier height U_0 decreases by half the change in the free energy ΔG_0. The value of a_0 changes accordingly.[30]

The energy (or temperature) dependence of $k(E)$ in the HBKB bound-continuum model is due only to the barrier properties U_0 and a_0 and not due to ΔG_0 since ρ is assumed to be constant with ΔG_0 [Eq. (6)]. The bound-bound tunneling models, on the other hand, predict an appreciable dependence of $k(E)$ on ΔG_0 [Eqs. (7) and (8) and Fig. 7]. Because the ρ term is energy dependent for the bound-bound models, but energy-independent for the bound-continuum model, the best choice of barrier parameters for matching the experimental values of $k(E)$ will be different for each model. In order to make a direct comparison between the models, we use a single value of U_0 (that reported for the bound-continuum model)[5] and accept for now that the bound-bound models are not optimized to the experimental data (although we adjusted a_0 slightly to 0.225 Å to normalize our first point to the $n = 3$ proton data as was done by HBKB). For the N–H, the O$\cdots$N, and the collective low frequency modes we assign frequencies of $\nu_H = 3000$ cm^{-1}, $\nu_N = 110$ and 99 cm^{-1} (for $n = 3$ and 4), and $\nu_L = 20$ cm^{-1}, respectively. The first two values are from HBKB[5] and the latter is an arbitrary value chosen to be significantly smaller than ν_N. Calculated rate constants were insensitive to the latter value over a tested range of 10–40 cm^{-1}. The coupling (reorganization energy) parameters λ_i are listed in the figure captions and are consistent with a value of about 4000 cm^{-1} measured for phenol-ammonia clusters (cf. Fig. 4). Nonetheless, they are rough estimates intended only illustrate the role of vibrations rather than to obtain quantitative information.

For $n = 3$ in Fig. 9, the solvent-activated bound-bound tunneling model predicts a decrease in $k(E)$ for small E followed by an increase at larger E. The downturn is a peculiarity of the solvent model that occurs for $\Delta G_0/\lambda_S \sim -1$ as seen in Fig. 7a. The energy dependence due to the O–H tunneling barrier

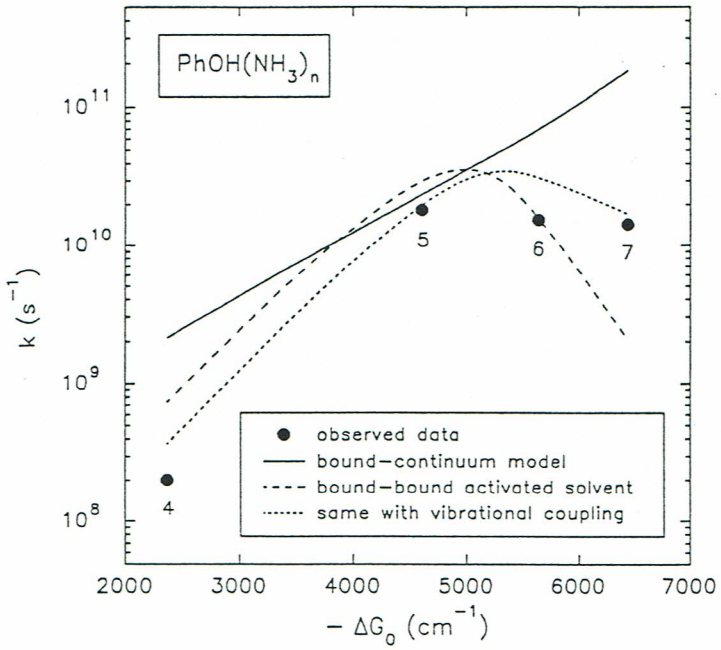

Figure 10. Calculated dependence of k on cluster size n and ΔG_0 by the three models of tunneling and comparison to measurements for $PhOH(NH_3)_n$. For simplicity we modeled only single mode coupling involving the O···N promoting and accepting stretch mode. Parameters for calculations ($n = 4 - 7$, respectively) are: $\nu_H = 3500$ cm^{-1} $\nu_N = 140$ cm^{-1}; $\mu_N = 23$ amu; $U_0 = 0.54, 0.40, 0.335, 0.285$ eV; $a_0 = 0.349, 0.30, 0.275, 0.253$ Å; $s = 6n - 6$; $E = 2500$ cm^{-1}, $k_bT = 13$ cm^{-1}, $\lambda_S = 4000$ cm^{-1}; $\lambda_N = 800$ cm^{-1}; $\Delta G_0 = -2360, -4600, -5640, -6440$ cm^{-1} (cf., Ref. 5 for explanation of frequency and barrier parameters).

dominates at larger E, which explains the upturn. The value of ΔG_0 used for $n = 3$ is consistent with the condition $-\Delta G_0/\lambda_S < 1$ for the unreactive $n = 2$ cluster. For $n = 4$, ΔG_0 decreases by about 0.3 eV as determined from stepwise solvation energies reported elsewhere.[6] Hence, ΔG_0 enters the inverted region where the activated-solvent model predicts very slow rates and a highly exaggerated $k(E)$ energy dependence. Including the coupling of product vibrations to the O–H coordinate overcomes this problem as illustrated in Fig. 9. A moderate and smoothly varying $k(E)$ energy dependence is obtained.

An important feature to note is that the bound-bound models are in better agreement with the absolute value of k for $n = 4$ better than is the bound-continuum model. This is seen more clearly in Fig. 10 where the calculated results are compared to the measured cluster size dependent rate constants for $PhOH(NH_3)_n$ (Fig. 9).[6] As noted in the Background section, the observation that k is relatively insensitive to n and ΔG_0 for 1-$NpOH(NH_3)_n$ and $PhOH(NH_3)_n$ was unexpected and at first difficult to explain. The bound-continuum model predicts an exponentially increasing k with ΔG_0 because the effect of changing ΔG_0 is due solely to the change in the tunneling barrier parameters U_0 and a_0. In the activated-solvent models an additional dependence on ΔG_0 appears in the solvent activation energy $\Delta G^{\ddagger}$. However, in the absence of product vibrational coupling, the dependence is exaggerated (Figs. 7a and 10). With vibrational coupling added to the model, the effect is moderated (Figs. 7b and 10) and more realistic. In this example, we used a single-mode treatment involving only ν_N.

7. SUMMARY AND CONCLUSIONS

Proton tunneling is strongly coupled to vibrational and solvent motion, however, the dependence is multidimensional and complex which makes the theory challenging. We have compared two previous models applied to clusters to a new model introduced here. Each model captures the importance of the O···N intermolecular mode for facilitating tunneling by modulating the O–H tunneling barrier width and height. The bound-continuum model is able to describe well the dependence on internal energy E, but not on ΔG_0. The bound-bound activated-solvent model has an excessive sensitivity to some parameters that can lead to predictions of extreme dependences on E and ΔG_0, although the model contains the necessary features to describe the ΔG_0 dependence. The inclusion of vibrational coupling moderates the harshness

of the activated solvent model. It should be noted that a simple single-mode calculation using just the O···N promoting and accepting mode, as used in Fig. 9, was able to give nearly as a good a description of experimental dependences as the multimode approach. A better method of treating vibrations should be explored once experimental measurements of important vibrational parameters become available. A number of other issues are left open; (1) the use of a Boltzmann factor for the solvent-activation is not strictly correct for the isoenergetic excitation of clusters, (2) the classical solvent coordinate is not valid in the limit of $E \rightarrow 0$, (3) The distinction between classical solvent modes and the low frequency quantal modes is not made sufficiently clear, (4) the dependence of the tunneling barrier properties on ΔG_0 is uncertain. This work would probably benefit from an effort to replace the classical solvent treatment leading to a Boltzmann expression with a semiclassical approach that considers a statistical probability of populating critical solvent modes.

Further experimental and theoretical work is needed to bridge our understanding of chemical dynamics from clusters to condensed-phase. The present account is a starting point for dealing with tunneling in small clusters where microcanonical conditions of constant energy and well-defined intermolecular vibrations are reasonable assumptions. To this we have added the concept of solvent-induced energy fluctuations. Further development should include extending and generalizing the treatment to permit a direct correspondence between clusters and thermal bulk phase.

8. REFERENCES

1. O. Cheshnovsky, and S. Leutwyler, *Chem. Phys. Lett.* **121,** 1 (1985). O. Cheshnovsky, and S. Leutwyler, *J. Chem. Phys.* **88,** 4127 (1988).

2. R. Knochenmuss and S. Leutwyler, *J. Chem. Phys.* **91,** 1268 (1989). T. Droz, R. Knochenmuss, and S. Leutwyler, *J. Chem. Phys.* **93,** 4520 (1990).

3. D. Solgadi, C. Jouvet, and A. Tramer, *J. Phys. Chem.* **92,** 3313 (1988). C. Jouvet, C. Lardeux-Dedonder, M. Richard-Viard, D. Solgadi, and A. Tramer, *J. Phys. Chem.* **94,** 5041 (1990).

4. J. J. Breen, L. W. Peng, D. M. Willberg, A. Heikal, P. Cong, and A. H. Zewail, *J. Chem. Phys.* **92,** 805 (1990).

5. M. F. Hineman, G. A. Bruker, D. F. Kelley, and E. R. Bernstein, *J. Chem. Phys.* **97,** 3341 (1992).

6. J. Steadman and J. A. Syage, *J. Chem. Phys.* **92,** 4630 (1990). J. A. Syage and J. Steadman, *J. Chem. Phys.* **95,** 2497 (1991).

7. J. Steadman and J. A. Syage, *J. Am. Chem. Soc.* **113,** 6786 (1991). J. A. Syage and J. Steadman, *J. Phys. Chem.* **96,** 9606 (1992).

8. J. Steadman and J. A. Syage, *J. Phys. Chem.* **95,** 10326 (1991).

9. J. A. Syage *J. Phys. Chem.* **97,** 12523 (1993).

10. J. A. Syage, *Chem. Phys. Lett.* **202,** 227 (1993). J. A. Syage, *Z. Phys. D.,* in press (1994).

11. R. Knochenmuss, G. R. Holtom, and D. Ray, *Chem. Phys. Lett.,* in press (1993).

12. M. F. Hineman, D. F. Kelley, and E. R. Bernstein, *J. Chem. Phys.* **99,** 533 (1993).

13. E. M. Kosower and D. Huppert, *Annu. Rev. Phys. Chem.* **37,** 127 (1986).

14. J. Lee, R. D. Griffin, and G. W. Robinson, *J. Chem. Phys.* **82,** 4920 (1985). J. Lee, G. W. Robinson, S. P. Webb, L. A. Philips, and J. H. Clark, *J. Am. Chem. Soc.* **108,** 6538 (1986).

15. D. H. Huppert, A. Jayaraman, R. G. Maines, Sr., D. W. Steyert, and P. M. Rentzepis, *J. Chem. Phys.* **81,** 5596 (1984).

16. D. C. Borgis, S. Lee, and J. T. Hynes, *Chem. Phys. Lett.* **162** 19 (1989). D. C. Borgis and J. T. Hynes, *Chem. Phys.* **170** 315 (1993). D. C. Borgis and J. T. Hynes, *J. Chem. Phys.* **94** 3619 (1991).

17. R. I. Cukier and M. Morillo, *J. Chem. Phys.* **91,** 857 (1990). M. Morillo and R. I. Cukier, *J. Chem. Phys.* **92,** 4833 (1990).

18. P. F. Barbara, G. C. Walker, and T. P. Smith, *Science,* **256,** 975 (1992).

19. J. A. Syage and J. Steadman, *Chem. Phys. Lett.* **166,** 159 (1990). J. Steadman, E. W. Fournier, and J. A. Syage, *Appl. Opt.* **29,** 4962 (1990).

20. J. A. Syage, in *Ultrafast Spectroscopy in Chemical Systems,* edited by J. D. Simon (Kluwer Academic Publishers, New York, 1993), p. 289. J. A. Syage, in *Femtosecond Chemistry,* edited by J. Manz and L. Wöste (VCH Publishers, New York, 1994).

21. J. Steadman and J. A. Syage, *Rev. Sci. Instrum.* **64,** 3094 (1993).

22. D. M. Willberg, M. Gutmann, J. J. Breen, and A. H. Zewail, *J. Chem. Phys.* **96,** 198 (1992). M. Gutmann, D. M. Willberg, and A. H. Zewail, *J. Chem. Phys.* **97,** 8037, 8048 (1992).

23. D. Ray, N. E. Levinger, J. M. Papanikolas, and W. C. Lineberger, *J. Chem. Phys.* **91,** 6533 (1989). J. M. Papanikolas, J. R. Gord, N. E. Levinger, D. Ray, V. Vorsa, and W. C. Lineberger, *J. Phys. Chem.* **95,** 8028 (1991).

24. M. P. Cassasa, J. C. Stephenson, and D. S. King, *J. Chem. Phys.* **89,** 1966 (1988). K. Fuke, K. Keizo, F. Misaizu, and K. Kaya, *J. Chem. Phys.* **95,** 4074 (1991).

25. S. Wei, J. Purnell, S. A. Buzza, R. J. Stanley, and A. W. Castleman, Jr., *J. Chem. Phys.* **97,** 9480 (1992). S. Wei, J. Purnell, S. A. Buzza, and A. W. Castleman, Jr., *J. Chem. Phys.* **99,** 755 (1993).

26. R. P. Bell, *The Tunnel Effect in Chemistry,* (Chapman-Hall, New York, 1980), Chap. 2.

27. R. A. Marcus, *Faraday Discuss. Chem. Soc.* **74,** 7 (1982).

28. G. L. Closs and J. R. Miller, *Science* **240,** 440 (1988).

29. J. Jortner and M. Bixon, *J. Chem. Phys.* **88,** 167 (1988). J. Ulstrup and J. Jortner, *J. Chem. Phys.* **63,** 4358 (1975). K. F. Freed, *Acc. Chem. Res.* **11,** 74 (1978).

30. If one assumes that only the amplitude, but not the curvature, of the inverted parabola changes with O$\cdots$N motion, then it follows that $U(x) = U_0(1 + x/2a_0)^2$ and $a(x) = a_0(1 + x/2a_0)$ where U_0 and a_0 are equilibrium values.

31. *Mathematica,* Wolfrum Research, Inc., 100 Trade Center Dr., Champaign, IL 61820-7237. Equations for $v = 1 - 5$ are available upon request.

32. P. J. and K. A. Holbrook, *Unimolecular Reactions,* (Wiley, New York, 1972).

33. S. Wei, W. B. Tzeng, and A. W. Castleman, Jr., *J. Phys. Chem.* **95,** 585 (1991).